ACS APPLIED NANO MATERIALS

www.acsanm.org Article

Surface Tension Nanogates for Controlled Ion Transport

Masoumeh Nazari, Sina Nazifi, Zixu Huang, Tian Tong, Habilou Ouro-Koura, Jiming Bao, Kausik Das, and Hadi Ghasemi*

Cite This: *ACS Appl. Nano Mater.* 2020, 3, 6979−6986 Read Online

ACCESS | Metrics & More | Article Recommendations | Supporting Information

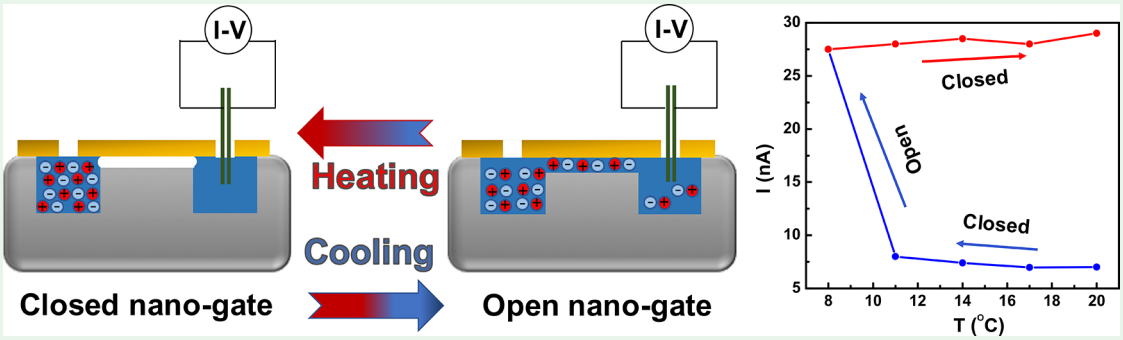

ABSTRACT: Capillary wicking drives liquid motion in miniature channels and capillaries, which are omnipresent in the human body, nature, and technology; examples include the brain's capillary network, plants, power systems, nanofluidics devices, and cooling systems for electronics/photonics. Capillary force is inversely proportional to the radius of confinement and becomes the dominant driving force for mass transport at smaller scales. Here, we demonstrate that capillary wicking breaks down at a sub-10 nm scale for some fluids, changing the governing physics of the mass transport and leading to a quasi-static liquid−vapor interface experiencing the dynamic process of wetting and liquid fracture in a cyclic manner. The scale of capillary breakdown is a function of interfacial tension of the liquid and could be tuned based on the system requirements. Capillary breakdown results in surface tension nanogates that are turned on/off via external stimuli such as minimal temperature actuation or applied voltage. These nanogates are highly effective and tunable for ion transport, playing a critical role in the functionality of biological systems. The surface tension nanogates promise platforms to govern nanoscale functionality of a wide spectrum of systems, and applications can be foreseen in drug delivery, energy conversion, power generation, seawater desalination, and ionic separation.

KEYWORDS: *nanochannels, capillary breakdown, nanogate, surface tension, ion/mass transport*

INTRODUCTION

Capillary force drives liquid flow in small channels and is the critical mechanism for mass transport in nature and technology.[1−3] In the human body, the brain's capillary network[4,5] controls blood flow and monitors neuronal activity and sweat glands' function based on capillary flow to regulate body temperature; in plants, transfer of water and nutrients from soil to the root and further to the leaves is possible through this governing force;[5−7] on earth, transport of water from aquifer to surface is achieved through capillary wicking;[8,9] in energy[10−13] or biological systems such as proton-exchange membrane fuel cells[14] and nanofluidics devices,[15−19] fluid transport in the confined channels is governed by this force;[20] in thermal management systems of electronics/photonics by heat pipes, spontaneous liquid transfer to the hot spot is also achieved through capillary force.[21−25]

On the other side, ion channels play a pivotal role in the human body through the control of ion flux across protein membranes[26] for a wide range of functions such as signal transduction, muscle development, release of neurotransmitters, hormone secretion, fever control, and brain function,[4,27−33] The capillary force (f_c) is governed by interfacial energies at the solid−liquid−vapor contact line and is inversely proportional to the dimension of the channel, d, and could be expressed as $f_c = F(\sigma^{SV},\sigma^{SL},\sigma^{LV},d)$, where σ is surface energy and superscripts SV, SL, and LV denote the solid−vapor, solid−liquid, and liquid−vapor interfaces, respectively.[34] That is, for a given set of surface energies, this force becomes dominant at small scale.[35,36]

Here, we demonstrated that despite being a dominant force at small scale, capillary force breaks down at sub-10 nm scale for some liquids and does not play any role in mass transport.

Received: May 12, 2020
Accepted: May 19, 2020
Published: May 19, 2020

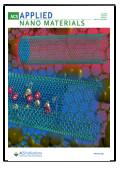

https://dx.doi.org/10.1021/acsanm.0c01304
ACS Appl. Nano Mater. 2020, 3, 6979−6986

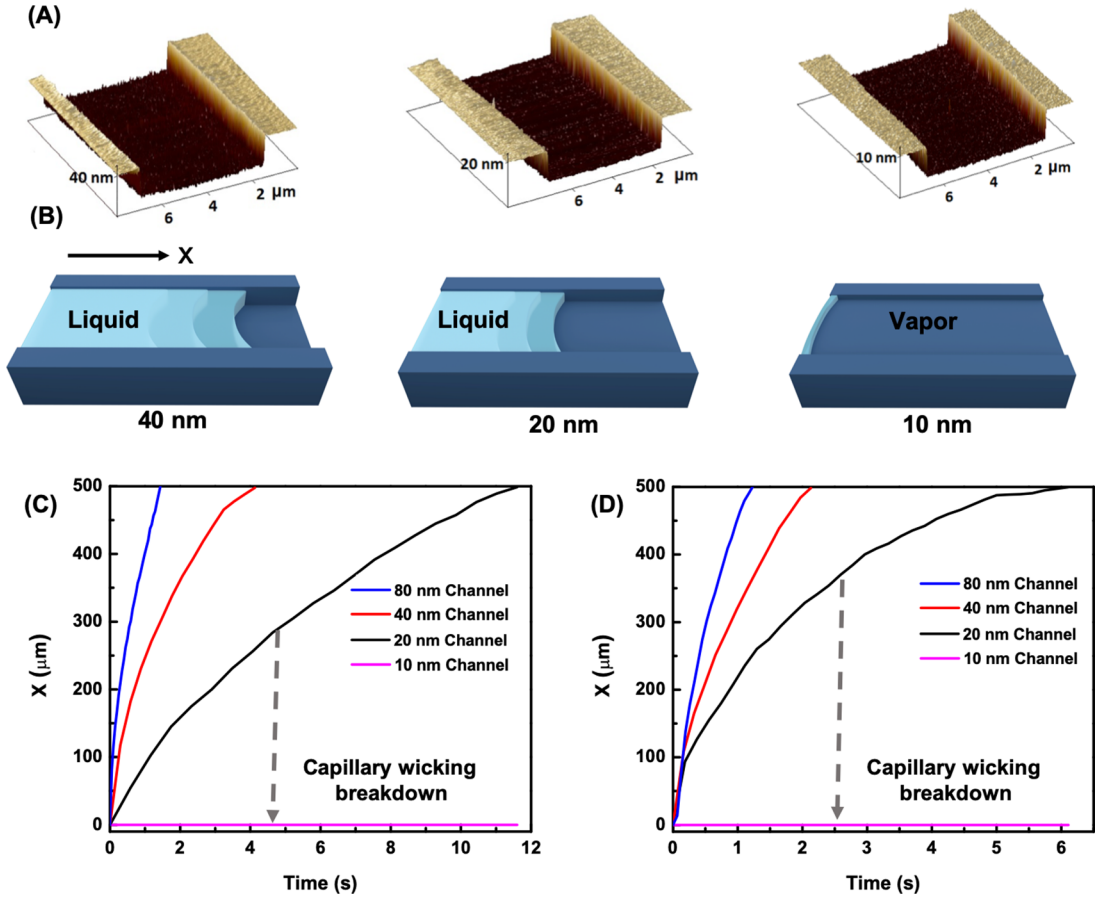

Figure 1. Capillary wicking in nanochannels. (a) Uniform profile of Si nanochannels probed with scanning probe microscopy (SPM). (b) Capillary wicking is observed in 40 and 20 nm channels, but the liquid front stays at a quasi-static state in the 10 nm channel. Temporal coordinates of (c) isopropanol and (d) ethanol wicking in 80, 40, and 20 nm indicate viscous motion in these channels. However, in the 10 nm channels, there is no liquid transport in the channels for both fluids.

At these scales, mass transport is governed through diffusion in the vapor phase, which is orders of magnitude slower than liquid flow. Once a liquid wets the walls of a small channel and forms a liquid–vapor interface, the formed net capillary force drives the liquid flow in the channel. However, at sub-10 nm scale, the liquid–vapor interface experiences a mechanically unstable state and goes through a fracture to vapor phase. The formed vapor phase is transported through diffusion, and the rewetting and fracture phenomenon occurs with high frequency for mass transport. We exploited this phenomenon to introduce the concept of surface tension nanogates, which are highly effective and tunable for ion transport. These channels could be activated and deactivated through any external stimulus that actuates surface tension, including temperature, electrical potential, and chemical composition. The ability to control mass and ion transport across nanoconfinement plays a significant role in a broad range of applications in biology, energy, and water systems.

RESULTS AND DISCUSSION

Nanochannels of Si with three selected depths of 40, 20, and 10 nm are developed through a nanofabrication process discussed in the Methods. Each nanofluidic chip includes 11 groups of channels with nine channels in each group, and each channel has a width of 5 μm and length of 500 μm. These nanochannels connect two large microreservoirs with a depth of 20 μm. The profile of each individual channel is probed with scanning probe microscopy (SPM) and is shown in Figure 1a and Supporting Information, Figure S1, l–n, confirming depth uniformity of the nanochannels. The nanochannels are sealed on top with a borosilicate glass through anodic bonding. It should be noted that, to prevent channel collapse due to high electrostatic force during anodic bonding, a 300 nm oxide film was thermally grown on silicon. After anodic bonding, the nanochannel survival was checked through some approaches discussed in the Methods. We chose isopropanol and ethanol as two working fluids with total wetting behavior on Si channels for this study. The flow of these liquids in the nanochannels is shown schematically in Figure 1b. For channels with depths of 40 and 20 nm, liquid wicks in the nanochannels, but for 10 nm channels, the liquid remains quasi-static at the channel's entrance with no motion. The temporal motion of liquids in these channels for isopropanol and ethanol is shown in Figure 1c,d and Supporting Information, S2. As shown, for 40 and 20 nm channels, the liquid is driven by capillary wicking, and its velocity is governed by a balance of capillary force and opposing viscous force, i.e., Washburn's equation. For these channels, the liquid motion deviates slightly from Washburn's equation[25,37,38] due to interfacial viscosity,[39−41] which is discussed in the Supporting Information, S3. However, for 10 nm channels, capillary wicking breaks down and there is no motion of liquid, even after a long time.

https://dx.doi.org/10.1021/acsanm.0c01304
ACS Appl. Nano Mater. 2020, 3, 6979−6986

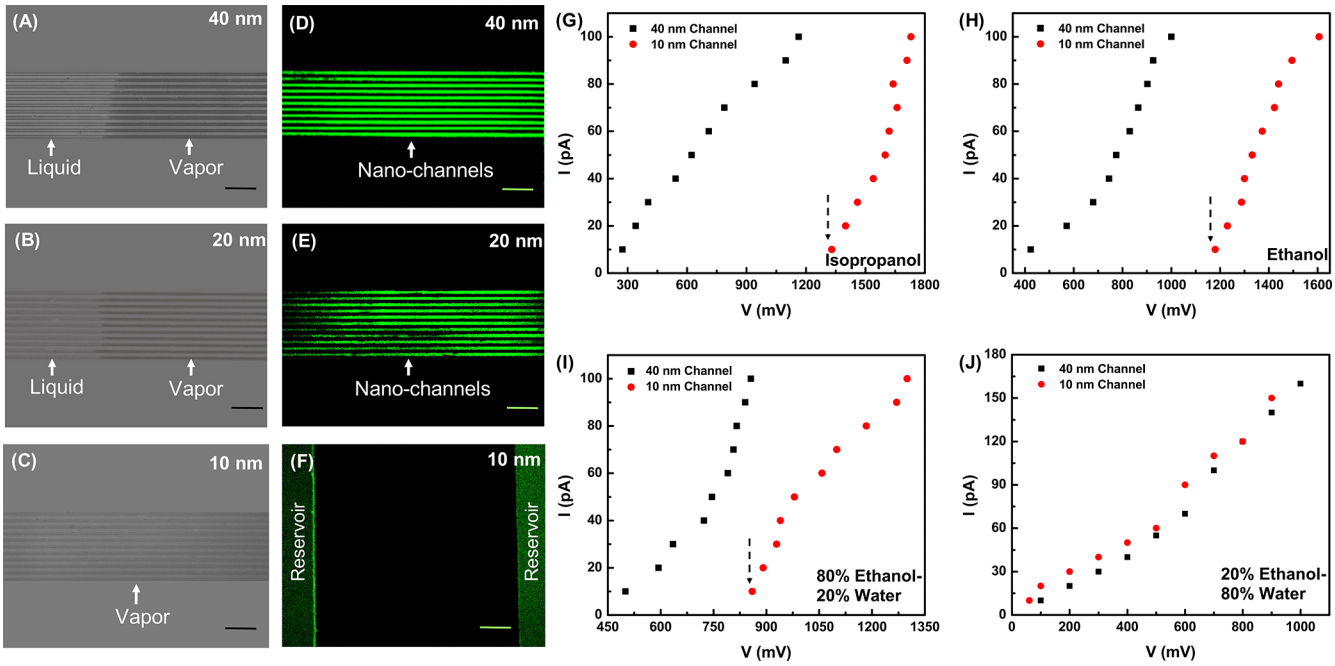

Figure 2. Capillary breakdown in sub-10 nm channels. (a–c) High-speed imaging of isopropanol transport in various nanochannels shows that there is no liquid flow in 10 nm channels and vapor phase fills the nanochannels between the microreservoirs. The scale bar is 50 μm. (d–f) The flow of isopropanol in the nanochannels is visualized through fluorescence microscopy. Despite liquid flow in deeper nanochannels, liquid does not transport in the 10 nm channels. The scale bar in (d, e) is 50 μm and in (f) is 80 μm. (g) $I-V$ curves across the nanochannels for isopropanol, suggesting two distinct behaviors for the 40 and 10 nm channels. For 40 nm channels, the $I-V$ curve suggests liquid conductance across the channels. However, for 10 nm channels, there is a threshold of electrical potential (1.33 V) between the microreservoirs before any conductance could be measured. As confirmed in another independent measurement, this threshold corresponds to electrical breakdown of the vapor phase, a proof of capillary breakdown at these scales. (h) Similar characteristics of capillary breakdown are observed with ethanol as the working fluid. (i) By tuning the surface tension of the working fluid, the threshold for electrical breakdown could be tuned. (j) As the surface tension of working fluid is increased, the capillary breakdown disappears, suggesting that this breakdown is a surface tension-dependent phenomenon. The arrows in panels g–i show the threshold of electrical potential (electrical breakdown of vapor).

We used three independent approaches to demonstrate capillary breakdown at a sub-10 nm scale. In the first approach, as shown in Figure 2a–c, we probed the motion of liquid in these nanochannels through coupled high-speed imaging and an optical microscope system, Supporting Information, S2. One of the microreservoirs was filled, and liquid transport was visualized in the nanochannels. Despite liquid flow in the 40 and 20 nm channels, no fluid motion was observed in the 10 nm channels. To achieve high-resolution imaging of the liquid phase in the 10 nm channels, we used wafers coated with 200 nm of Si_3N_4 through chemical vapor deposition;[38] see Supporting Information, S4. The Si_3N_4 shows a strong Fabry–Perot resonance in reflection, resulting in a sharp contrast between ultrathin liquid and vapor phase.[42] In the second approach, we used fluorescence microscopy to visualize liquid motion in the nanochannels; see Supporting Information, S5. As shown in Figure 2d–f, the liquid flow is evident in the 40 and 20 nm channels, but no liquid flow occurs in the 10 nm channel. In the third approach, we used $I-V$ curves to examine the liquid motion in the nanochannels. In these experiments, one microreservoir was filled, and liquid was allowed to wick to the other microreservoir. The other microreservoir was then completely filled. For the case of 10 nm channels, both microreservoirs were filled with the working fluid. Two electrodes were placed in the microreservoirs, with no contact with the walls of the microreservoirs, and $I-V$ curves in the channels were measured; see Supporting Information, S6. The $I-V$ curve for pure isopropanol is shown in Figure 2g, which indicates two distinct characteristics for 40 and 10 nm channels. The calculated electrical conductivity of both 40 and 10 nm channels is 1×10^{-10}–2.7×10^{-10} S/m. However, for the 10 nm channel, there is a threshold of electrical potential before any current in the channels could be measured. That is, an insulator phase exists in these channels. We conducted these experiments for ethanol, Figure 2h, and the same behavior for 40 and 10 nm channels were observed with electrical conductivity of 1.7×10^{-10}–2.3×10^{-10} S/m. One common physical property of these two liquids is their low surface tension (22.1–23 mN m^{-1}).[43] In the next set of experiments, we tuned the surface tension of the working liquid to the value of 24 mN m^{-1} through a mixture of 80% ethanol–20% water, Figure 2i. Similar characteristics were observed for the 40 and 10 nm channels. The surface tension of the liquid was further increased to 38 mN m^{-1} through a mixture of 20% ethanol–80% water, Figure 2j. Interestingly for this working fluid, the $I-V$ curves of 40 and 10 nm channels overlap, with electrical conductivity of 5.7×10^{-10}–6.2×10^{-10} S/m. That is, the existence of an electrically insulating phase in these channels is a function of the surface tension of the working fluid. To understand the threshold electrical potential in $I-V$ curves, we designed an experimental setup to determine electrical breakdown of ethanol and isopropanol vapor phases; see Supporting Information, S7. These independent experiments suggest electrical breakdown of 2.7 and 1.91 kV m^{-1} for isopropanol and ethanol vapor, respectively. As nanochannels are 500 μm in length, the breakdown voltage in 10 nm nanochannels is 1.35 V for isopropanol and 0.955 V for

https://dx.doi.org/10.1021/acsanm.0c01304
ACS Appl. Nano Mater. 2020, 3, 6979–6986

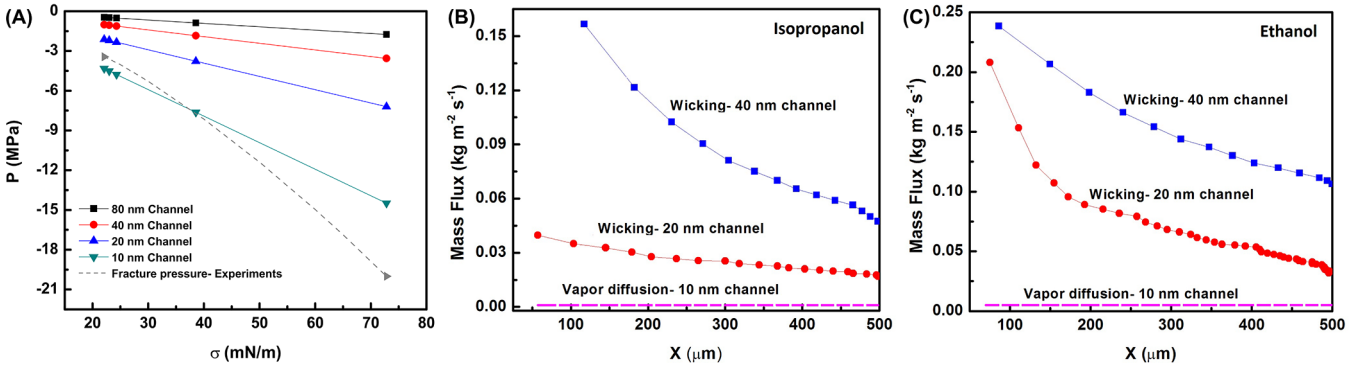

Figure 3. Scale-dependent mass transport mechanism. (a) The liquid pressure in different nanochannels for studied fluids. The experimental limit of liquid fracture as a function of surface tension (i.e., $\sim\sigma_{LV}^{3/2}$) is depicted by a dashed line. For the scenarios in which the liquid pressure in nanochannels falls below the limit of liquid fracture, wicking breakdown is observed. The mass flux for different length scales is shown for (b) isopropanol and (c) ethanol. Although for 40 and 20 nm channels capillary wicking is the transport mechanism, at 10 nm channels vapor diffusion governs mass transport, with several orders of magnitude lower flux, 0.001 kg m^{-2} s^{-1} for isopropanol and 0.005 kg m^{-2} s^{-1} for ethanol.

ethanol. These voltage breakdowns are consistent with the measured breakdowns in Figure 2g,h. That is, the capillary wicking breaks down at these channels with only vapor phase between microreservoirs. Note that we just used $I-V$ characteristic as a precise method to explore the existence of liquid−vapor phase in the nanochannels and not to drive wetting[44] (i.e., electro-wetting). As suggested by Figure 2j, the length scale for capillary breakdown is a function of surface tension of the liquid. To further analyze this effect, we studied deionized (DI) water flow in the nanochannels, due to its high surface tension, through fluorescence microscopy, Supporting Information, S8. The results suggest that atm 10 nm nanochannels, water wicks in the channels. However, the liquid flow may not be as uniform as the other liquids due to partial wetting of the channel walls with DI water. Capillary wicking of water in sub-10 nm confinements has been also observed by other researcher.[s19,20,45,46] These experiments confirm that the surface tension of the liquid plays a critical role in capillary wicking breakdown. This fact has been also demonstrated in a study performed by Duan et al.[47] They measured electrical conductivity of 2 nm silica nanochannels filled with ethanol and DI water, and observed that ethanol-filled nanochannels provided nearly zero conductance, while water-filled nanochannels showed quite high values. Since the electrical conductance values of bulk ethanol and DI water are in the same order of magnitude (are almost similar), and the conductance mechanism in both liquids is the same, one can conclude that the small conductance value of ethanol-filled nanochannels comes from vapor phase occupying the nanochannels.

We determined the liquid pressure at the wicking front through the Laplace equation (see Supporting Information, S9 and Table S2) for nanochannels with different depths and for five studied types of liquids, as shown in Figure 3a. As shown, the value of liquid pressure falls in the absolute negative pressure domain[48−52] due to the high curvature of the liquid−vapor interface. The state of negative liquid pressure is a thermodynamically unstable state, but could be a mechanically stable state up to a spinodal decomposition limit. The limit of negative pressure for liquids, given by Fisher,[53] is proportional to $\sigma_{LV}^{3/2}$; see Supporting Information, S10. Although the theoretical limit of liquid fracture is at extreme negative pressures, the measured experimental values are at moderate negative pressures. The measured experimental limits of liquid fracture for ethanol and water[53,54] are depicted in Figure 3a, and the data are interpolated through a $\sigma_{LV}^{3/2}$ curve. This limit for liquid fracture falls above the liquid pressure in 10 nm channels for isopropanol, ethanol, and 80% ethanol−20% water. That is, the liquid in these channels experiences an unstable mechanical state and goes through fracture to a vapor phase. In other words, no stable liquid−vapor interface could be formed for these fluids in 10 nm channels. The kinetics of wetting of these channels is governed by interfacial energies and viscous dissipation at the meniscus region; see Supporting Information, S11. As the liquid from microreservoirs wets the channels' wall, curvature of the liquid−vapor interface increases, pushing the liquid pressure to lower negative values until it reaches the fracture limit. Through the kinetics of wetting, we determined the time scale required to reach the fracture limit, which is approximately 28 ns—the process of wetting and fracture occurs so fast! The frequency of liquid fracture is not sensitive to the fracture pressure and could be as low as 1 fs. We could not detect this frequency with high-speed imaging. Both wicking and diffusion have time dependence of $t^{1/2}$.[55] The diffusion coefficient for vapor self-diffusion is on the order of 10^{-9} m^2/s, and interestingly this coefficient for the wicking process is on the same order; see Supporting Information, S12 and Table S3. That is, the volumetric transport by both processes is the same, but the mass transport is different based on the density ratio of liquid and vapor. As there is no equilibrium for the liquid wetting and fracture, this process occurs in a cyclic fashion for mass transport in these channels. We determined the mass flux in these channels for the discussed length scales, as shown in Figure 3b,c and Supporting Information, S13, for both isopropanol and ethanol. As indicated, mass flux can be reduced by a few orders of magnitude due to capillary breakdown at sub-10 nm scales.

As the capillary breakdown leads to a change of the mass transport mechanism from liquid wicking to vapor diffusion, we explored this physical concept to develop a new generation of ion channels. The currently known ion channels are ligand-gated, mechanically gated, and voltage-gated.[56−58] Ion transfer through the liquid phase could be significantly faster than that through the vapor phase. To demonstrate these novel ion channels, we chose temperature as the external stimulus to actuate surface tension. A fluid mixture of 50% ethanol−50% water was chosen for these nanogates, as a transition between

https://dx.doi.org/10.1021/acsanm.0c01304
ACS Appl. Nano Mater. 2020, 3, 6979−6986

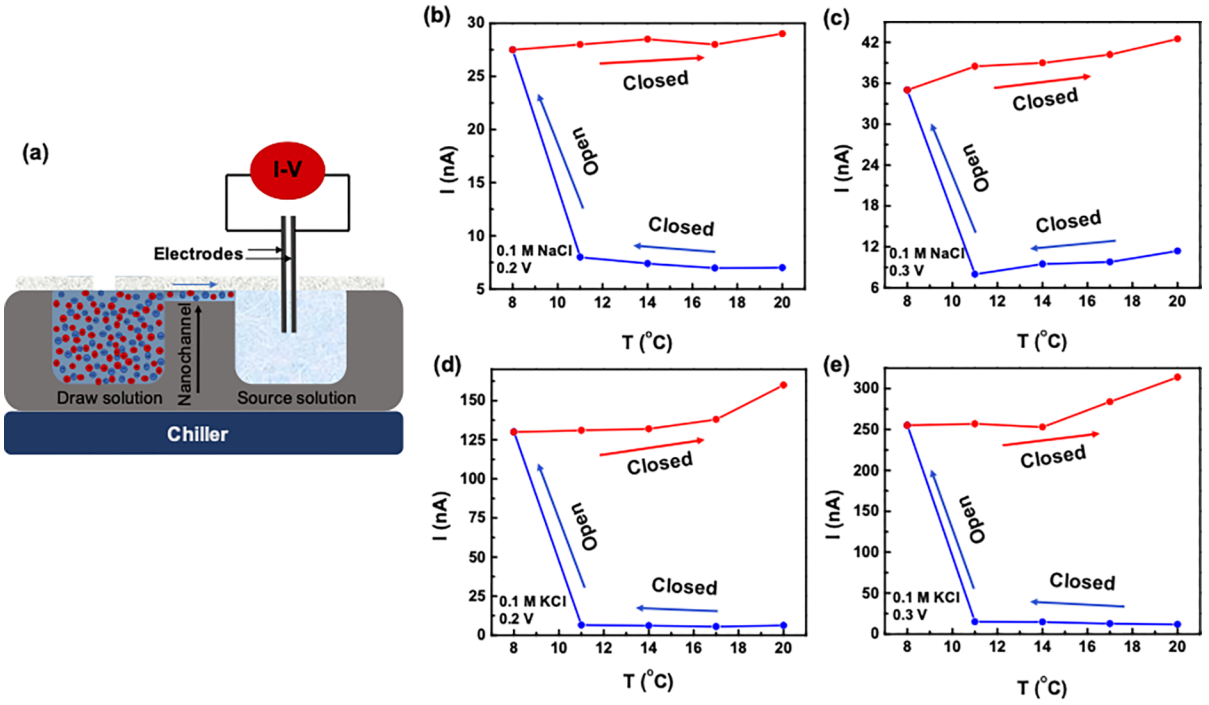

Figure 4. Surface tension nanogates. (a) Experimental setup for demonstration of nanogates performance. (b, c) Transport of ions is activated and deactivated in 10 nm channels through temperature modulation. Initially, microreservoir (1) is a liquid solution with 0.1 M NaCl, and microreservoir (2) is a pure fluid. The conductance in microreservoir (2) is shown as a function of temperature. At ambient temperature, the nanochannels are closed for ion transport and conductance is minimal. As the temperature of the nanochannels is reduced to a threshold value, surface tension increases, leading to opening of the gate and capillary wicking between the microreservoirs, and consequently ion transport from microreservoir (1) to microreservoir (2). This leads to a sharp rise in conductance. As the temperature of the nanochannels is increased back, the gates are closed again with no further ion transport. (d, e) Surface tension gate characteristics are demonstrated for KCl solution at different applied voltages.

liquid fracture and wicking could occur by small surface tension changes; see Supporting Information, S14. A set of Si nanochannels with a depth of 10 nm was chosen for these nanogates. Microreservoir (1) was filled with a solution of 0.1 M NaCl, and microreservoir (2) was filled with a pure liquid. We used ionic conductance measurements in microreservoir (2) to demonstrate the performance of these surface tension nanogates, as shown in Figure 4a. At room temperature, the nanogates are closed as the vapor phase exists in these nanochannels. We incrementally decreased the temperature of the nanochannels from room temperature to 11 °C, as shown in Figure 4b,c. There was a minimal change in conductance of microreservoir (2), but no ion transport was detected. As the temperature of nanochannels was decreased to 8 °C, there was a sharp boost in the conductance of microreservoir (2), indicating open nanogates and transport of ions by diffusion. Once the temperature of the nanochannels was increased again, the conductance became approximately constant, with no further change, indicating closed nanogates. The further slight increase in conductance is due to a temperature effect, as shown in the Supporting Information, S14 and Figure S9b. These ion nanogates could be activated and deactivated by any means that could tune surface tension. To further show these nanogates, we show the transport of K^+ and Cl^- across these ion gates in Figure 4d,e. Similar to Na^+ ions, the gating characteristics could be achieved by temperature modulations. The activation of nanogates is also demonstrated through fluorescence microscopy in the Supporting Information, Figure S10.

CONCLUSIONS

In summary, despite being the dominant force at small scale, capillary wicking breaks down at sub-10 nm scale and plays no role in mass transport. The breakdown length depends on the interfacial tensions at the solid−liquid−vapor contact line. As the liquid contact line advances in sub-10 nm channels to wet the surface, the liquid could experience an unstable state of negative pressure due to the high curvature of the liquid−vapor interface and fracture to vapor phase. The liquid−vapor interface adopts a quasi-static state in which the processes of wetting and fracture occur in a cyclic fashion. The mass flux at these scales is governed by vapor diffusion, which is orders of magnitude slower than capillary wicking. This breakdown leads to the concept of surface tension nanogates. These gates could be turned on/off by any means that actuate surface tension. The transport of Na^+ and K^+ ions across these gates is demonstrated. This new type of efficient and tunable ion gate offers a new avenue for controlled mass transport and promises extensive implementation in drug delivery, molecular separation, energy conversion, power generation, and seawater desalination.

METHODS

Device Fabrication. The fabrication process consists of four main steps, including patterning, etching, thermal oxide growing, and anodic bonding, as presented in the Supporting Information, Figure S1, a−k. First, a positive photoresist was uniformly dispersed on a silicon wafer by using a spin coater (Brewer Cee 200) and then baked on a hot plate at 130 °C for 90 s. In order to create an optical mask, the geometric pattern of the nanochannels was designed in

https://dx.doi.org/10.1021/acsanm.0c01304
ACS Appl. Nano Mater. 2020, 3, 6979−6986

SolidWorks (Dassault Systemes) and transferred onto a chrome mask with a resolution of 1 μm. The optical mask was utilized to pattern the photoresist by exposing it to UV irradiation through a mask aligner (ABM). Afterward, the sample was immersed into a photoresist developer, washed with DI water, and dried with nitrogen flow. Our structure includes nine sets of nanochannels bridging two microreservoirs. Each set of nanochannels consists of 11 individual nanochannels. The width and length of each nanochannel are 5 and 500 μm, respectively. The nanochannels' patterns were etched into the silicon wafer with different depths using controlled reactive ion etching (Oxford Plasma Lab ICP 180 RIE). To remove the photoresist after etching, the sample was washed with acetone, alcohol, and DI water, and then dried with nitrogen flow. The channels height is in the range of 10−500 nm, which can be defined by the etching recipe of silicon. All the steps of standard photolithography and reactive ion etching were repeated to pattern and etch two microreservoirs perpendicularly located at the two ends of nanochannels. The microreservoirs are squares with length of 4 mm and height of 20 μm. In the next step, 300 nm oxide was thermally grown on the developed micronanochannels. This thermal oxide acts as an insulating layer which decreases the high electro-static forces in nanometer distances between silicon and glass and prevents channel collapse during anodic bonding. We confirmed the thickness of the thermal oxide layer through an ellipsometry method. The last step of nanofluidic device fabrication is sealing the developed micronanochannels with borosilicate glass through an anodic bonding process. Initially, two holes were drilled on the glass in order to facilitate the introduction of liquid to the microreservoirs. Next, the silicon wafer and borosilicate glass were dipped into piranha solution (H_2SO_4:H_2O_2 = 3:1) for 15 min. After cleaning, the silicon wafer and borosilicate glass were bonded together by an anodic bonding process carried out for 10 min at 400 °C with a voltage of 300 V. To check nanochannels' survival after anodic bonding, first we observed the bonded nanofluidic chip with an optical microscope. The successful bonding was indicated by a uniform color across the whole length and width of the nanochannels (an example of partially collapsed channels is shown in the Supporting Information, Figure S1, p). We also measured the electrical conductance of nanochannels filled with liquid to further explore the channels' survival. In open channels, changing current as a function of voltage was observed, while no current could be detected for the blocked channels. It should be noted that 300 nm thermal oxide prevented current leakage through our nanofluidic chip during conductance measurements.

■ ASSOCIATED CONTENT

Supporting Information

The Supporting Information is available free of charge at https://pubs.acs.org/doi/10.1021/acsanm.0c01304.

Characterization of nanochannels, capillary wicking experimental setup, Washburn's equation, silicon nitride nanochannels, fluorescence (confocal) microscopy - isopropanol flow, electrical conductance measurement setup, electrical breakdown measurement setup, fluorescence microscopy - water flow, calculation of liquid pressure through the Young−Laplace equation, fracture of liquid, kinetics of wetting in nanochannels, coefficient of wicking process and determination of mass flux, vapor transport in 10 nm nanochannels and its mass flux calculations, and surface tension nanogates (PDF)

■ AUTHOR INFORMATION

Corresponding Author

Hadi Ghasemi − *Department of Mechanical Engineering, University of Houston, Houston, Texas 77204, United States;* orcid.org/0000-0002-0554-4248; Email: hghasemi@uh.edu

Authors

Masoumeh Nazari − *Department of Mechanical Engineering, University of Houston, Houston, Texas 77204, United States*

Sina Nazifi − *Department of Mechanical Engineering, University of Houston, Houston, Texas 77204, United States*

Zixu Huang − *Department of Mechanical Engineering, University of Houston, Houston, Texas 77204, United States*

Tian Tong − *Department of Electrical and Computer Engineering, University of Houston, Houston, Texas 77204, United States*

Habilou Ouro-Koura − *Department of Physics, University of Maryland Eastern Shore, Princess Anne, Maryland 21853, United States; Department of Mechanical Engineering, Rensselaer Polytechnic Institute, Troy, New York 12180, United States*

Jiming Bao − *Department of Electrical and Computer Engineering, University of Houston, Houston, Texas 77204, United States;* orcid.org/0000-0002-6819-0117

Kausik Das − *Department of Physics, University of Maryland Eastern Shore, Princess Anne, Maryland 21853, United States*

Complete contact information is available at: https://pubs.acs.org/10.1021/acsanm.0c01304

Author Contributions

H.G. and M.N conceived the idea. M.N., S.N., T.T., and H.O. conducted the breakdown experiments. M.N. and Z.H. conducted nanogates experiments. M.N. fabricated the nanofluidic device. M.N. and H.G. wrote the manuscript with input from all the authors. J.B. and K.D. commented on the manuscript. H.G. directed the research.

Funding

H.G. received funding from the Air Force Office of Scientific Research (Grant AFOSR FA9550-16-1-0248) with Dr. Ali Sayir as program manager and National Science Foundation (Grant NSF-1804204). K.D. received funding from the National Science Foundation (HBCU-UP Award No. 1719425) and the Department of Education (MSEIP Award No. P120A70068) with MSEIP CCEM Supplemental award. The work was partly done at the Texas Nanofabrication Facility supported by NSF grant NNCI-1542159.

Notes

The authors declare the following competing financial interest(s): A provisional patent is filed on the concept of surface tension-gated channels. Hadi Ghasemi is co-founder of Surfellent LLC.

■ ACKNOWLEDGMENTS

We thank Hamid Fekri for helping in image processing, and Bahareh Eslami and Parham Jafari for helping in the experiments.

■ REFERENCES

(1) Bonn, D.; Eggers, J.; Indekeu, J.; Meunier, J.; Rolley, E. Wetting and Spreading. *Rev. Mod. Phys.* **2009**, *81* (2), 739−805.

(2) Choi, J.; Ghaffari, R.; Baker, L. B.; Rogers, J. A. Skin-Interfaced Systems for Sweat Collection and Analytics. *Sci. Adv.* **2018**, *4* (2), eaar3921.

(3) Supple, S.; Quirke, N. Rapid Imbibition of Fluids in Carbon Nanotubes. *Phys. Rev. Lett.* **2003**, *90* (21), 214501.

(4) Longden, T. A.; Dabertrand, F.; Koide, M.; Gonzales, A. L.; Tykocki, N. R.; Brayden, J. E.; Hill-Eubanks, D.; Nelson, M. T. Capillary K+-Sensing Initiates Retrograde Hyperpolarization to

Increase Local Cerebral Blood Flow. *Nat. Neurosci.* **2017**, *20* (5), 717−726.
(5) Wheeler, T. D.; Stroock, A. D. The Transpiration of Water at Negative Pressures in a Synthetic Tree. *Nature* **2008**, *455*, 208−212.
(6) Ha, J.; Kim, J.; Jung, Y.; Yun, G.; Kim, D. N.; Kim, H. Y. Poro-Elasto-Capillary Wicking of Cellulose Sponges. *Sci. Adv.* **2018**, *4* (3), eaao7051.
(7) Wang, Y.; Lee, J.; Werber, J. R.; Elimelech, M. Capillary-Driven Desalination in a Synthetic Mangrove. *Sci. Adv.* **2020**, *6* (8), eaax5253.
(8) Koos, E.; Willenbacher, N. Capillary Forces in Suspension Rheology. *Science (Washington, DC, U. S.)* **2011**, *331* (6019), 897−900.
(9) Bocquet, L.; Charlaix, E.; Ciliberto, S.; Crassous, J. Moisture-Induced Ageing in Granular Media and the Kinetics of Capillary Condensation. *Nature* **1998**, *396*, 735−737.
(10) Feng, J.; Graf, M.; Liu, K.; Ovchinnikov, D.; Dumcenco, D.; Heiranian, M.; Nandigana, V.; Aluru, N. R.; Kis, A.; Radenovic, A. Single-Layer MoS2 Nanopores as Nanopower Generators. *Nature* **2016**, *536* (7615), 197−200.
(11) Zhang, Z.; Sui, X.; Li, P.; Xie, G.; Kong, X. Y.; Xiao, K.; Gao, L.; Wen, L.; Jiang, L. Ultrathin and Ion-Selective Janus Membranes for High-Performance Osmotic Energy Conversion. *J. Am. Chem. Soc.* **2017**, *139* (26), 8905−8914.
(12) Van Der Heyden, F. H. J.; Stein, D.; Dekker, C. Streaming Currents in a Single Nanofluidic Channel. *Phys. Rev. Lett.* **2005**, *95* (11), 116104.
(13) Ghaffarizadeh, S. A.; Zandavi, S. H.; Ward, C. A. Specific Surface Area from Nitrogen Adsorption Data at 77 K Using the Zeta Adsorption Isotherm. *J. Phys. Chem. C* **2017**, *121* (41), 23011−23016.
(14) Banham, D.; Kishimoto, T.; Zhou, Y.; Sato, T.; Bai, K.; Ozaki, J. I.; Imashiro, Y.; Ye, S. Critical Advancements in Achieving High Power and Stable Nonprecious Metal Catalyst-Based MEAs for Real-World Proton Exchange Membrane Fuel Cell Applications. *Sci. Adv.* **2018**, *4* (3), eaar7180.
(15) Bocquet, L. Nanofluidics: Bubbles as Osmotic Membranes. *Nat. Nanotechnol.* **2014**, *9* (4), 249−251.
(16) Bocquet, L.; Charlaix, E. Nanofluidics, from Bulk to Interfaces. *Chem. Soc. Rev.* **2010**, *39* (3), 1073−1095.
(17) Radha, B.; Esfandiar, A.; Wang, F. C.; Rooney, A. P.; Gopinadhan, K.; Keerthi, A.; Mishchenko, A.; Janardanan, A.; Blake, P.; Fumagalli, L.; Lozada-Hidalgo, M.; Garaj, S.; Haigh, S. J.; Grigorieva, I. V.; Wu, H. A.; Geim, A. K. Molecular Transport through Capillaries Made with Atomic-Scale Precision. *Nature* **2016**, *538* (7624), 222−225.
(18) Holt, J. K.; Park, H. G.; Wang, Y.; Stadermann, M.; Artyukhin, A. B.; Grigoropoulos, C. P.; Noy, A.; Bakajin, O. Sub-2-Nanometer Carbon Nanotubes. *Science* **2006**, *312* (May), 1034−1038.
(19) Holt, J. K.; Park, H. G.; Wang, Y.; Stadermann, M.; Artyukhin, A. B.; Grigoropoulos, C. P.; Noy, A.; Bakajin, O. Fast Mass Transport Through Sub-2-Nanometer Carbon Nanotubes. *Science (Washington, DC, U. S.)* **2006**, *312* (5776), 1034−1037.
(20) Xie, Q.; Alibakhshi, M. A.; Jiao, S.; Xu, Z.; Hempel, M.; Kong, J.; Park, H. G.; Duan, C. Fast Water Transport in Graphene Nanofluidic Channels. *Nat. Nanotechnol.* **2018**, *13* (3), 238−245.
(21) Nazari, M.; Masoudi, A.; Jafari, P.; Irajizad, P.; Kashyap, V.; Ghasemi, H. Ultrahigh Evaporative Heat Fluxes in Nanoconfined Geometries. *Langmuir* **2019**, *35* (1), 78−85.
(22) Cho, H. J.; Preston, D. J.; Zhu, Y.; Wang, E. N. Nanoengineered Materials for Liquid-Vapour Phase-Change Heat Transfer. *Nat. Rev. Mater.* **2017**, *2* (2), 16092.
(23) Farokhnia, N.; Sajadi, S. M.; Irajizad, P.; Ghasemi, H. Decoupled Hierarchical Structures for Suppression of Leidenfrost Phenomenon. *Langmuir* **2017**, *33* (10), 2541−2550.
(24) Farokhnia, N.; Irajizad, P.; Sajadi, S. M.; Ghasemi, H. Rational Micro/Nanostructuring for Thin-Film Evaporation. *J. Phys. Chem. C* **2016**, *120* (16), 8742−8750.
(25) Alibakhshi, M. A.; Xie, Q.; Li, Y.; Duan, C. Accurate Measurement of Liquid Transport through Nanoscale Conduits. *Sci. Rep.* **2016**, *6* (March), 24936.
(26) Sun, Y.; Chen, S.; Chen, X.; Xu, Y.; Zhang, S.; Ouyang, Q.; Yang, G.; Li, H. A Highly Selective and Recyclable NO-Responsive Nanochannel Based on a Spiroring Opening-closing Reaction Strategy. *Nat. Commun.* **2019**, *10* (1), 1323.
(27) Nguyen, P. T.; DeMarco, K. R.; Vorobyov, I.; Clancy, C. E.; Yarov-Yarovoy, V. Structural Basis for Antiarrhythmic Drug Interactions with the Human Cardiac Sodium Channel. *Proc. Natl. Acad. Sci. U. S. A.* **2019**, *116* (8), 2945−2954.
(28) Hutson, M. R.; Keyte, A. L.; Hernández-Morales, M.; Gibbs, E.; Kupchinsky, Z. A.; Argyridis, I.; Erwin, K. N.; Pegram, K.; Kneifel, M.; Rosenberg, P. B.; Matak, P.; Xie, L.; Grandl, J.; Davis, E. E.; Katsanis, N.; Liu, C.; Benner, E. J. Temperature-Activated Ion Channels in Neural Crest Cells Confer Maternal Fever-Associated Birth Defects. *Sci. Signaling* **2017**, *10* (500), eaal4055.
(29) Saotome, K.; Murthy, S. E.; Kefauver, J. M.; Whitwam, T.; Patapoutian, A.; Ward, A. B. Structure of the Mechanically Activated Ion Channel Piezo1. *Nature* **2018**, *554* (7693), 481−486.
(30) Jensen, M.; Jogini, V.; Borhani, D. W.; Leffler, A. E.; Dror, R. O.; Shaw, D. E. Mechanism of Voltage Gating in Potassium Channels. *Science (Washington, DC, U. S.)* **2012**, *336* (6078), 229−233.
(31) Yellen, G. The Voltage-Gated K+ Channels and Their Relatives. *Nature* **2002**, *419* (Sept), 35−42.
(32) Burns, J. R.; Seifert, A.; Fertig, N.; Howorka, S. A Biomimetic DNA-Based Channel for the Ligand-Controlled Transport of Charged Molecular Cargo across a Biological Membrane. *Nat. Nanotechnol.* **2016**, *11* (2), 152−156.
(33) Zhang, Z.; Wen, L.; Jiang, L. Bioinspired Smart Asymmetric Nanochannel Membranes. *Chem. Soc. Rev.* **2018**, *47* (2), 322−356.
(34) Israelachvili, J. N. *Intermolecular and Surface Forces*, 3rd ed.; Academic Press: New York, 2010.
(35) Xue, Y.; Markmann, J.; Duan, H.; Weissmüller, J.; Huber, P. Switchable Imbibition in Nanoporous Gold. *Nat. Commun.* **2014**, *5* (May), 4237.
(36) Kelly, S.; Balhoff, M. T.; Torres-Verdín, C. Quantification of Bulk Solution Limits for Liquid and Interfacial Transport in Nanoconfinements. *Langmuir* **2015**, *31* (7), 2167−2179.
(37) De Gennes, P.-G.; Brochard-Wyart, F.; Quéré, D. *Capillarity and Wetting Phenomena: Drops, Bubbles, Pearls, Waves*; Springer Science & Business Media, 2004.
(38) Li, H.; Zhong, J.; Pang, Y.; Zandavi, S. H.; Persad, A. H.; Xu, Y.; Mostowfi, F.; Sinton, D. Direct Visualization of Fluid Dynamics in Sub-10 Nm Nanochannels. *Nanoscale* **2017**, *9* (27), 9556−9561.
(39) Zhu, Y.; Granick, S. Viscosity of Interfacial Water. *Phys. Rev. Lett.* **2001**, *87*, 096104.
(40) Israelachvili, J.; Wennerstrom, H. Role of Hydration and Water Structure in Biological and Colloidal Interactions. *Nature* **1996**, *379*, 219−225.
(41) Kelly, S.; Torres-Verdín, C.; Balhoff, M. T. Anomalous Liquid Imbibition at the Nanoscale: The Critical Role of Interfacial Deformations. *Nanoscale* **2016**, *8* (5), 2751−2767.
(42) Van Delft, K. M.; Eijkel, J. C. T.; Mijatovic, D.; Druzhinina, T. S.; Rathgen, H.; Tas, N. R.; Van Den Berg, A.; Mugele, F. Micromachined Fabry-Pérot Interferometer with Embedded Nano-channels for Nanoscale Fluid Dynamics. *Nano Lett.* **2007**, *7* (2), 345−350.
(43) Vazquez, G.; Alvarez, E.; Navaza, J. M. Surface Tension of Alcohol + Water from 20 to 50 °C. *J. Chem. Eng. Data* **1995**, *40* (3), 611−614.
(44) Smirnov, S. N.; Vlassiouk, I. V.; Lavrik, N. V. Voltage-Gated Hydrophobic Nanopores. *ACS Nano* **2011**, *5* (9), 7453−7461.
(45) Alibakhshi, M. A.; Xie, Q.; Li, Y.; Duan, C. Accurate Measurement of Liquid Transport through Nanoscale Conduits. *Sci. Rep.* **2016**, *6*, 24936.
(46) Haneveld, J.; Tas, N. R.; Brunets, N.; Jansen, H. V.; Elwenspoek, M. Capillary Filling of Sub- 10 Nm Nanochannels. *J. Appl. Phys.* **2008**, *104*, 014309.
(47) Duan, C.; Majumdar, A. Anomalous Ion Transport in 2-Nm Hydrophilic Nanochannels. *Nat. Nanotechnol.* **2010**, *5* (12), 848−852.

https://dx.doi.org/10.1021/acsanm.0c01304
ACS Appl. Nano Mater. 2020, 3, 6979−6986

(48) Zheng, Q.; Durben, D. J.; Wolf, G. H.; Angell, C. a. Liquids at Large Negative Pressures: Water at the Homogeneous Nucleation Limit. *Science* **1991**, *254* (5033), 829−832.
(49) Green, J. L.; Durben, D. J.; Wolf, G. H.; Angell, C. A. Water and Solutions at Negative Pressure: Raman Spectroscopic Study to −80 Megapascals. *Science (Washington, DC, U. S.)* **1990**, *249* (4969), 649−652.
(50) Versluis, M.; Schmitz, B.; Von der Heydt, A.; Lohse, D. How Snapping Shrimp Snap: Through Cavitating Bubbles. *Science (Washington, DC, U. S.)* **2000**, *289* (5487), 2114−2117.
(51) Duan, C.; Karnik, R.; Lu, M.-C.; Majumdar, A. Evaporation-Induced Cavitation in Nanofluidic Channels. *Proc. Natl. Acad. Sci. U. S. A.* **2012**, *109* (10), 3688−3693.
(52) Xiao, R.; Maroo, S. C.; Wang, E. N. Negative Pressures in Nanoporous Membranes for Thin Film Evaporation. *Appl. Phys. Lett.* **2013**, *102* (12), 123103.
(53) Fisher, J. C. The Fracture of Liquids. *J. Appl. Phys.* **1948**, *19*, 1062−1067.
(54) Caupin, F.; Herbert, E. Cavitation in Water: A Review. *C. R. Phys.* **2006**, *7* (9−10), 1000−1017.
(55) Jafari, P.; Masoudi, A.; Irajizad, P.; Nazari, M.; Kashyap, V.; Eslami, B.; Ghasemi, H. Evaporation Mass Flux: A Predictive Model and Experiments. *Langmuir* **2018**, *34* (39), 11676−11684.
(56) Wang, J.; Fang, R.; Hou, J.; Zhang, H.; Tian, Y.; Wang, H.; Jiang, L. Oscillatory Reaction Induced Periodic C-Quadruplex DNA Gating of Artificial Ion Channels. *ACS Nano* **2017**, *11* (3), 3022−3029.
(57) Guan, W.; Li, S. X.; Reed, M. A. Voltage Gated Ion and Molecule Transport in Engineered Nanochannels: Theory, Fabrication and Applications. *Nanotechnology* **2014**, *25* (12), 122001.
(58) Li, H.; Qiu, C.; Ren, S.; Dong, Q.; Zhang, S.; Zhou, F.; Liang, X.; Wang, J.; Li, S.; Yu, M. Na+-Gated Water-Conducting Nanochannels for Boosting CO2 Conversion to Liquid Fuels. *Science (Washington, DC, U. S.)* **2020**, *367* (6478), 667−671.

https://dx.doi.org/10.1021/acsanm.0c01304
ACS Appl. Nano Mater. 2020, 3, 6979−6986